nature communications



Article

https://doi.org/10.1038/s41467-025-60848-5

Non-monotonic size-dependent exciton radiative lifetime in CsPbBr₃ nanocrystals

Received: 14 September 2024

Accepted: 5 June 2025

Published online: 11 July 2025



Abdullah S. Abbas 1,8,10 , Daniel Chabeda 2,10 , Daniel Weinberg 2,3 , David T. Limmer 2,3,4 , Eran Rabani 2,3,5 & A. Paul Alivisatos 1,2,3,6,7,8,9

Lead halide perovskite nanocrystals have attracted intense interest due to their desirable optical properties, diverse structural features, and size-tunable excitonic structure. Here we show that, under ambient conditions, a nonmonotonic trend in radiative lifetime emerges from the interplay of size, lattice symmetry and excitonic structure. Small nanocrystals exhibit long radiative lifetimes due to weakly emissive excitons, but the oscillator strength increases and shortens the lifetime for nanocrystals approaching intermediate confinement. For larger nanocrystals with higher exciton density of states (DOS), the radiative lifetime is lengthened due to depopulation of the bright exciton manifold into thermally accessible dim states. A size-dependent structural symmetry lowering transition from cubic to orthorhombic is observed by XRD and MD simulations, and the non-monotonic radiative lifetime trend emerges only in lower symmetry structures with an increased dim exciton DOS. These findings shed light on the impact of nanocrystal size and structure on radiative lifetime and pave the way for tailored optical materials in various optical applications.

Colloidal nanocrystals, also known as quantum dots (QDs), have attracted considerable attention due to their straightforward and inexpensive solution-phase synthesis and their wide-range spectral tunability from the quantum confinement effect^{1,2}. Lead halide perovskite nanocrystals, in particular cesium lead bromide (CsPbBr₃), have emerged in the past few years as highly desirable and efficient optical materials due to their facile synthesis, narrow emission linewidth, and near-unity photoluminescence quantum yield (PLQY) owing to their low trap density and tolerance for shallow surface defects³⁻¹². The photoluminescence quantum yield is in part dictated by the radiative lifetime, or the time between generation and radiative recombination of an exciton. Nanocrystals with near-unity PLQY and short radiative lifetimes have possible applications in coherent quantum light emitters¹³ and solid-state laser cooling¹⁴. For

example, to observe laser cooling in solid-state materials, two processes must occur in rapid succession: exciton up-conversion followed by radiative recombination, resulting in anti-Stokes photoluminescence¹⁴. A shorter radiative lifetime enhances the likelihood of avoiding non-radiative pathways that induce heating, thereby maximizing the cooling probability. One way to tune the radiative lifetime is through the nanocrystal size^{15,16}. For nanocrystals, three distinct quantum confinement regimes dictated by the Bohr radius—weak, intermediate, and strong—are commonly observed. Each regime exhibits a unique electronic structure and optical properties, influencing factors such as the radiative lifetime. Notably, CsPbBr₃ nanocrystals have a relatively large Bohr diameter (-7 nm), enabling experimental exploration across all three confinement regimes³.

¹Department of Materials Science and Engineering, University of Berkeley, Berkeley, CA, USA. ²Department of Chemistry, University of California, Berkeley, CA, USA. ³Materials Sciences Division, Lawrence Berkeley National Laboratory, CA, USA. ⁴Kavli Energy NanoScience Institute, Berkeley, CA, USA. ⁵The Raymond and Beverly Sackler Center of Computational Molecular and Materials Science, Tel Aviv University, Tel Aviv, Israel. ⁶Pritzker School of Molecular Engineering, The University of Chicago, Chicago, IL, USA. ⁷James Franck Institute, The University of Chicago, Chicago, IL, USA. ⁸Present address: Department of Chemistry, The University of Chicago, Chicago, IL, USA. ⁹Present address: Department of Chemistry and Pritzker School of Molecular Engineering, The University of Chicago, Chicago, IL, USA. ¹⁰These authors contributed equally: Abdullah S. Abbas, Daniel Chabeda. e-mail: paul.alivisatos@uchicago.edu

Previous work investigating size-dependent lifetimes in CsPbBr₃ under low temperature conditions (-4-5 K) revealed an exponential trend, with the radiative lifetime decreasing as the size increased^{13,15}. Under ambient conditions, however, the work of Krieg et al. shows the reverse trend¹⁶. It was rationalized that higher lying states become thermally accessible at ambient conditions and introduce a delay in the radiative recombination of excitons¹⁶. Neither of these studies thoroughly explored the inflection point marking the transition from the intermediate to the strong confinement regime. By exploring this inflection, size-dependent non-monotonicity was observed with a mechanism that relies on behavior common among intensively studied II-VI (CdSe)¹⁷⁻²⁰ and perovskite semiconducting nanocrystals, signifying potential design criteria for optimal recombination properties.

In this work, we explore the effect of nanocrystal size on radiative lifetime under ambient conditions. High-quality CsPbBr₃ nanocrystals were synthesized to ensure monoexponential decay behaviors, enabling direct extraction of the radiative lifetime. Unexpectedly, we observe a non-monotonic trend in the radiative lifetime. The smaller nanocrystals within the strong confinement regime and larger nanocrystals approaching weak confinement exhibited long radiative lifetimes, while intermediately confined nanocrystals display the shortest radiative lifetime. A microscopic mechanism was explored by solving the Bethe-Salpeter equation (BSE) to obtain excitons in lead halide perovskite nanocrystals, having obtained electron and hole states from atomistic pseudopotential calculations. Strongly confined nanocrystals exhibit long radiative lifetimes due to their small oscillator strengths. For larger nanocrystals approaching the weak confinement regime, atomistic quasiparticle + BSE calculations predict a dense manifold of non-emissive dim excitons that, at room temperature, thermally depopulate the low energy bright triplet excitons. Distinctly, intermediately confined nanocrystals exhibit the shortest radiative lifetime due to the balance of enhanced oscillator strength compared to small nanocrystals and reduced thermal depopulation compared to weakly confined nanocrystals. This observation finds support from a previous work where the lengthening of radiative lifetime is attributed to the mixing of S state with higher P state that are symmetry forbidden¹⁶. Analysis of the present result in comparison to Krieg et al. is presented in Figure S1.

Additionally, we observed a symmetry lowering transition from the cubic to orthorhombic structures²¹⁻²⁵ of CsPbBr₃ nanocrystal system by both X-ray diffraction (XRD) patterns and molecular dynamics (MD) simulations. However, the onset of symmetry lowering (2 nm) did not coincide with the nanocrystal sizes where non-monotonicity in the lifetimes was observed (5–6 nm). Thus, we do not directly attribute the non-monotonic lifetimes to this transition. Rather, the non-monotonicity emerges from the size-dependent excitonic structure and only parametrically depends on the nanocrystal structural symmetry. This study leverages high-quality synthesis and advanced computational capabilities to provide a thorough and systematic insight into the size-dependent radiative lifetime in CsPbBr₃ nanocrystals, paving the way to engineer materials with tailored decay rates to meet diverse optical application needs.

Results

We investigated the effect of nanocrystal size on optical properties, focusing on the radiative lifetime. Over 30 high-quality nanocrystals samples were synthesized following a modified version of previous reports (details in the Method section) to minimize non-radiative pathways and to directly extract the radiative lifetime. Figure 1a shows absorption and photoluminescence spectra of CsPbBr₃ nanocrystals in the strong, intermediate, and weak confinement regime. Figure 1c-e show their corresponding Transmission Electron Microscopy (TEM) images (larger area shown in Figure S2) along with calculated size distributions²⁶, illustrating highly monodisperse ensemble. Photoluminescence Full-Width at Half Maximum (FWHM) and Stokes shift are extracted for different nanocrystal sizes revealing a linear trend. Both the FWHM and Stokes shift exhibit an increase as nanocrystal sizes decrease, which

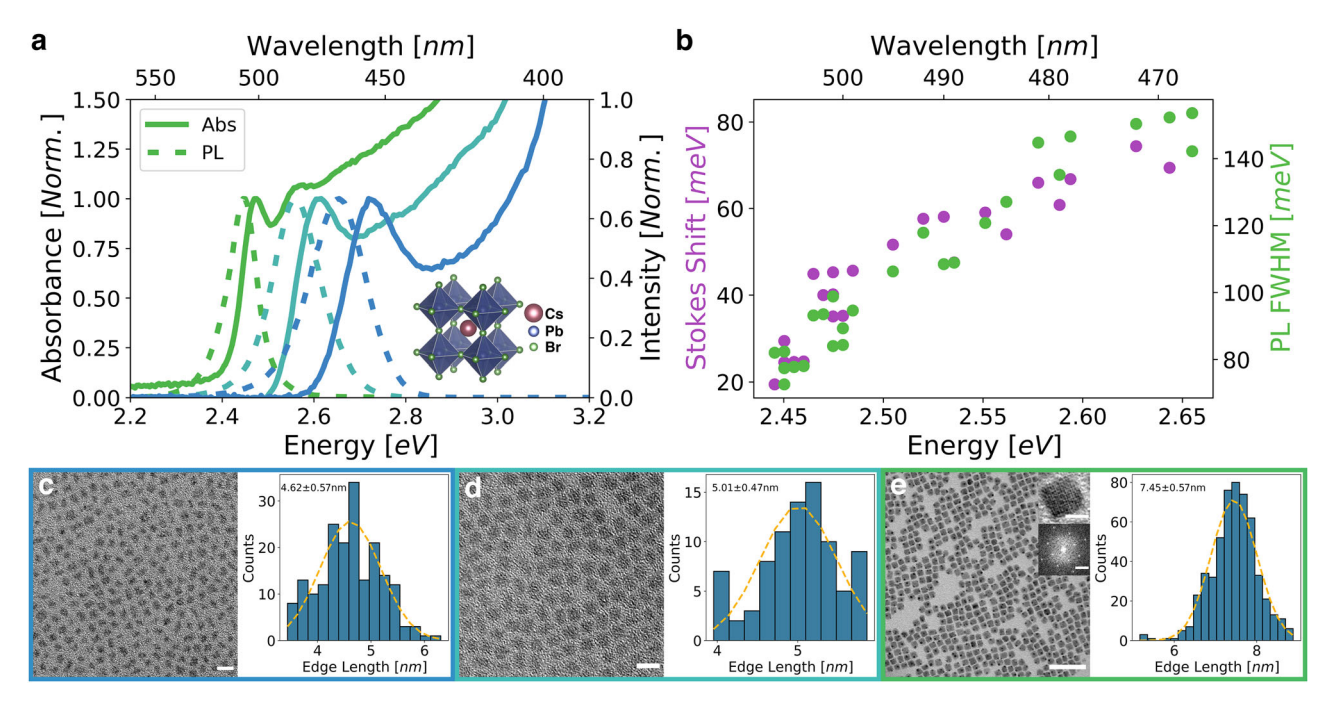


Fig. 1 | **Optical and structural characterizations of CsPbBr₃ nanocrystals with varying sizes. a** steady-state absorption, and photoluminescence (PL) spectra of selected nanocrystals in weak, intermediate, and strong quantum confinement regime, with inset showing the crystal structure created with Vesta³⁸. **b** Stokes shift and full width at half max as a function of bandgap energy are plotted displaying a linearly increasing trend as nanocrystal sizes decrease. **c**-**e** are transmission

electron microscope (TEM) images along with their corresponding size distributions fitted with gaussian curve to extract the average nanocrystal size. TEM images scale bars are as follow: (c) 10 nm, (d) 10 nm, and (e) 50 nm with inset showing high resolution TEM of a single nanocrystal with 5 nm scale bar and its corresponding Fast Fourier Transform (FFT) with 2 nm⁻¹ scale bar.

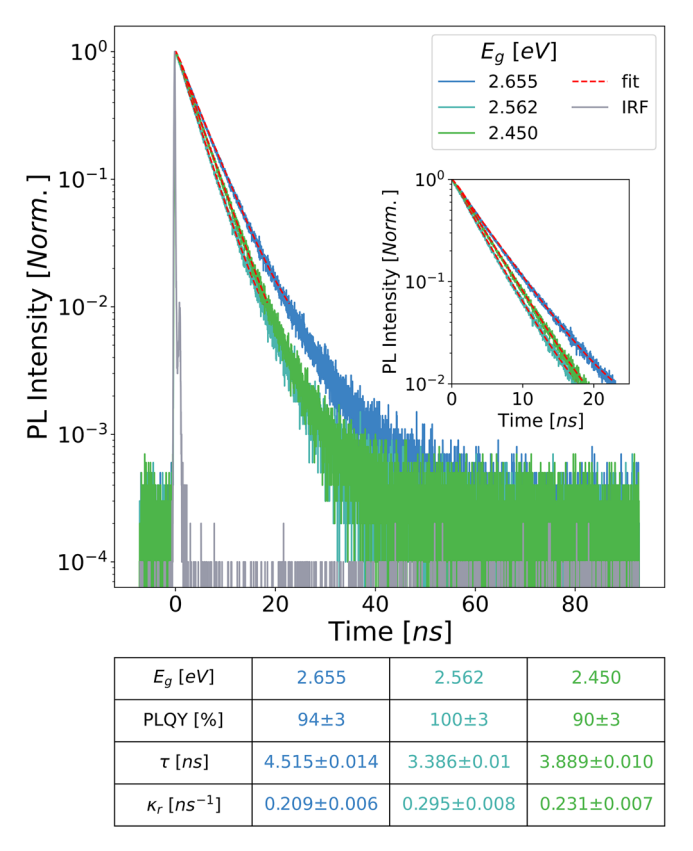


Fig. 2 | **Time-resolved photoluminescence (TRPL) characterization.** Three selected nanocrystals sizes in strong, intermediate, and strong quantum confinement regimes are assessed using TRPL. Decays are deconvoluted with instrument response function (IRF) and the initial two decades are fitted to a monoexponential function to extract the total lifetime (inset). Absolute photoluminescence quantum yield (PLQY) was measured to calculate the radiative rates for each nanocrystals. The resulting data, including bandgap (E_g), PLQY, total lifetime, and radiative rate, are tabulated, revealing a non-monotonic trend that emerges in lifetimes and radiative rates.

has been observed previously^{27,28}. This linear trend is correlated between the size of the nanocrystals and the strength of coupling to high-energy optical phonons (2–17 meV)^{28,29}. Specifically, smaller nanocrystals exhibit stronger coupling to these phonons due to enhanced charge density and subsequent polaron formation³⁰. This coupling results in large fluctuations in the bandgap³¹, consequentially causing broader emission linewidths and larger Stokes shift as evident in Fig. 1a and b.

Each synthesized distinct nanocrystal sample underwent characterization to determine photoluminescence quantum yield (PLQY) and time-resolved photoluminescence (TRPL) to quantify the radiative lifetime (τ_r) , which is inversely related to the radiative rate (κ_r) , using the following relation:

$$PLQY = \frac{\frac{1}{\tau_r}}{\frac{1}{\tau_r} + \frac{1}{\tau_{nr}}} = \frac{\frac{1}{\tau_r}}{\frac{1}{\langle \tau \rangle}} \tag{1}$$

$$\tau_r = \frac{\langle \tau \rangle}{PLQY} \tag{2}$$

$$\kappa_r = \frac{1}{\tau_r} \tag{3}$$

where $\langle \tau \rangle$ is total lifetime extracted by deconvoluting with the instrument response function (IRF) and subsequentially fitting the initial two

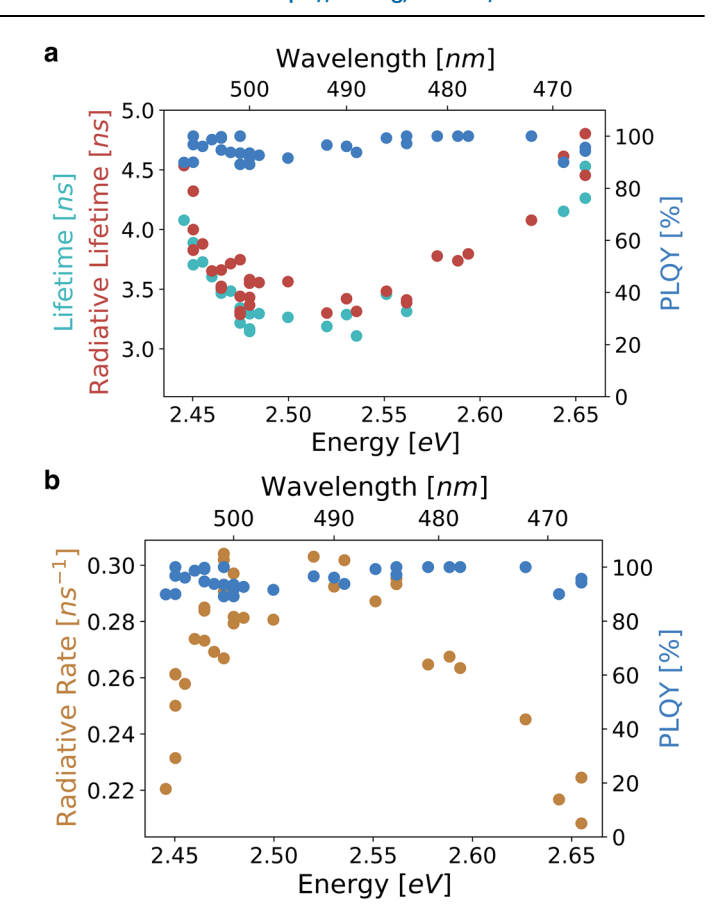


Fig. 3 | **Size-dependent exciton radiative lifetimes and rates of CsPbBr3 nanocrystals. a** Measured total lifetime under ambient conditions along with calculated radiative lifetimes via the absolute photoluminescence quantum yield (PLQY) as a function of nanocrystal size exhibit an unexpected non-monotonic trend. Larger nanocrystals in weak confinement regime show lengthened radiative lifetimes that decrease as the nanocrystal size transition into the intermediate confinement regime. Surprisingly, the trend reverses with decreasing nanocrystals size reaching the strong confinement regime. **b** radiative rates, the inverse of radiative lifetimes, showcasing an optimal size associated with maximum radiative rate.

decades of TRPL decays, as shown in Fig. 2, using a monoexponential function as follow:

$$I(t) = \int_{-\infty}^{t} IRF(t')^*A e^{-\frac{t-t'}{t}} dt'$$
 (4)

The tabulated data in Fig. 2 show the near-unity PLQY CsPbBr₃ nanocrystals across the three confinement regimes. Notably, the strongly and weakly confined nanocrystals exhibit longer radiative lifetime (or slower radiative rate) compared to the intermediately confined nanocrystals.

We conducted further measurements of PLQY and TRPL across different nanocrystal sizes within each of the three confinement regimes under ambient conditions (Supplementary Figs. S3, and S4). Surprisingly, our findings reveal a non-monotonic trend in both radiative lifetime and radiative rate, as shown in Fig. 3a and b. We find, in confirmation of earlier reports¹⁶, that the weakly confined nanocrystals exhibit longer radiative lifetimes. Unexpectedly, our measurements on strongly confined nanocrystals display similar long radiative lifetimes. Interestingly, we observe the shortest radiative lifetimes within the intermediate confinement regime. Thus, there exists some optimal nanocrystal size for applications where fast radiative recombination is desirable.

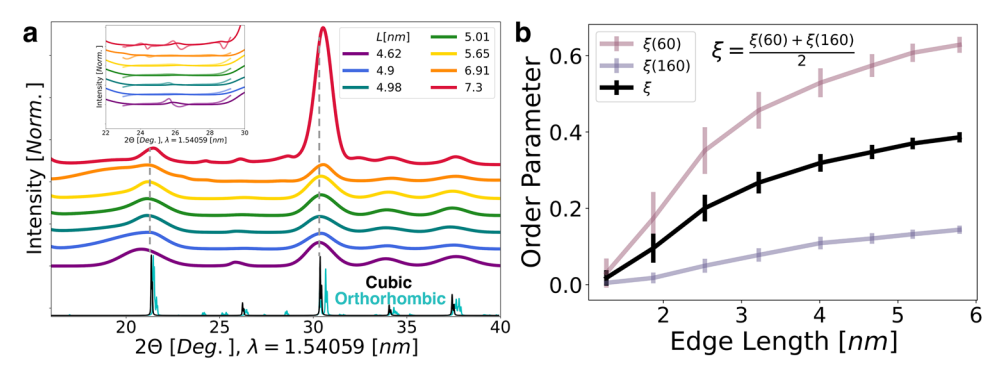


Fig. 4 | X-ray diffraction (XRD) and molecular dynamics (MD) of varying $CsPbBr_3$ nanocrystal sizes. a XRD patterns illustrating the transition from cubic to orthorhombic symmetry. b a composite order parameter that assesses the degree of crystal phase computed from MD simulation trajectories under ambient conditions in reference to a perfect cubic and orthorhombic symmetry, where 0

indicates a cubic and 1 means an orthorhombic symmetry. Error bars denote the variance of the order parameter due to fluctuations in 100 sampled geometries over the simulation. The order parameter results align with XRD patterns, confirming the size-dependent phase transition from being cubic in small nanocrystals to orthorhombic in larger nanocrystals.

To understand the underlying factors that may contribute to the lengthened radiative lifetime, we delved into a comprehensive examination of the crystal structure. In Fig. 4a, the powder X-ray diffraction (XRD) patterns of the nanocrystals with sizes spanning the three confinement regimes are illustrated. The nanocrystals in the strong confinement regime exhibit a cubic phase. As the size of the nanocrystals increases, a transition into an orthorhombic phase is observed^{21–25}. This phase transition, as discussed below, is further corroborated by molecular dynamics simulations at 300 K, as shown in Fig. 4b.

Molecular dynamics simulations as implemented in LAMMPS were performed on CsPbBr₃ nanocubes with edge lengths of 2-6 nm using a previously parametrized force field^{32,33}. The average structural symmetry at 300 K was computed over nanosecond simulation lengths to resolve the size-dependent phase behavior. To produce a quantitative metric of the structural symmetry, we define a local order parameter, ξ , that distinguishes the common cubic and orthorhombic phases of CsPbBr₃ nanocrystals. The order parameter is defined on the probability distribution of nearest neighbor halide-halide-halide (X-XX) angles of the nanocrystal configuration.

$$\xi_{i}(\theta) = \frac{[P_{i}(\theta) - P_{cubic}^{\circ}(\theta)]^{2}}{[P_{ortho}^{\circ}(\theta) - P_{cubic}^{\circ}(\theta)]^{2}}$$
 (5)

where $P_i(\theta)$ is the probability of finding an X-X-X angle of θ in the i-th trajectory step, and $P^{\circ}(\theta)$ is the probability of observing angle θ in the perfectly symmetric structure. If the configuration along the trajectory possesses cubic symmetry, then the order parameter becomes zero. If the configuration is orthorhombic, the ratio of terms is unity, and the order parameter is one. The averaged order parameter for a certain size, $\langle \xi(\theta) \rangle$, is estimated over the simulation trajectory, and we compare it against perfectly cubic and orthorhombic nanocubes of the same size.

The probability distribution of X-X-X angles distinguishes strongly between cubic and orthorhombic CsPbBr₃ at two angles, 60° and 160° . For perfectly cubic perovskites, 1/6 of the angles are 60° while zero angles are 60° for perfectly orthorhombic structures. This is reversed at 160° , where perfectly cubic structures have no probability and orthorhombic structures have a 1/6 probability. Supplementary Figure S5 shows histograms illustrating the probabilities, allowing for a clear distinction of certain angles that specifically emerge in one phase but are absent in the other. We develop a composite measure of the size-dependent phase behavior of perovskite nanocrystals in our simulations by averaging $\xi(60^{\circ})$ and $\xi(160^{\circ})$ over a narrow angular bin:

$$\xi = \frac{\xi(60^{\circ}) + \xi(160^{\circ})}{2}.$$
 (6)

As evident in Fig. 4b, the smaller nanocrystals, characterized by strong quantum confinement, display a cubic structure. As the nanocrystals size increases, a transition occurs, with the average nanocrystal structure progressively shifting towards orthorhombic symmetry–results that closely align with the experimental XRD patterns shown in Fig. 4a. Simulations were also performed on analogous CsPbl₃ perovskite nanocrystals and a similar phase behavior was observed. Comparative analysis of the size-dependent anisotropy for CsPbBr₃ and CsPbl₃ nanocrystals is presented in Supplementary Fig. S6.

Further theoretical understanding of the interplay between perovskite structural and optical properties was gained by performing atomistic electronic structure calculations on the relaxed structures for varying nanocrystal sizes. Accurate electron and hole quasiparticle states including spin-orbit coupling effects were computed within the semi-empirical pseudopotential framework as described in previous reports (Supplementary Fig. S7)34. We obtain a validated pseudopotential from Weinberg et al. describing local, nonlocal and spin-orbit coupling effects for CsPbI₃³⁴. Electron-hole correlation was included by solving the Bethe-Salpether equation (BSE) within the static screening approximation, which describes excitons in the basis of electron-hole product states³⁵. The electronic properties of CsPbI₃ and CsPbBr₃ show analogous trends³⁶; thus, we compute radiative lifetimes using the validated CsPbI₃ model as a proxy to understand the measured CsPbBr₃ radiative lifetimes. Massively parallel software implementations were developed to enable investigation of nanocrystals spanning the strong to intermediately confined regimes, with edge lengths ranging from 2-7 nm. In addition to systems with cubic and orthorhombic symmetry, we relax nanocrystal structures at 0 K using the previously parametrized force field to obtain static input geometries³². It was verified that the 0 K structures show the same size dependent phase behavior as the 300 K simulations (Supplementary Fig. S6). This gives us three structures to compare for each size: cubic, orthorhombic, and relaxed.

We calculated the thermally averaged radiative lifetime in the time-dependent perturbation theory framework as:

$$\langle \tau_r \rangle = \frac{1}{\langle \kappa_r \rangle} = \left[\frac{1}{Z} \sum_n e^{-\beta E_n} \frac{\omega_n^3 |\mu_n|^2}{3\pi \varepsilon_o \hbar c^3} \right]^{-1}$$
 (8)

where ε_o , \hbar , c are the vacuum permittivity, reduced Planck's constant, and speed of light, respectively. The parameters ω_n and μ_n correspond to the transition frequency and the transition dipole strength of exciton n. Reported radiative lifetimes are the Boltzmann thermal average over excitons. An exciton basis consisting of a few thousand electron

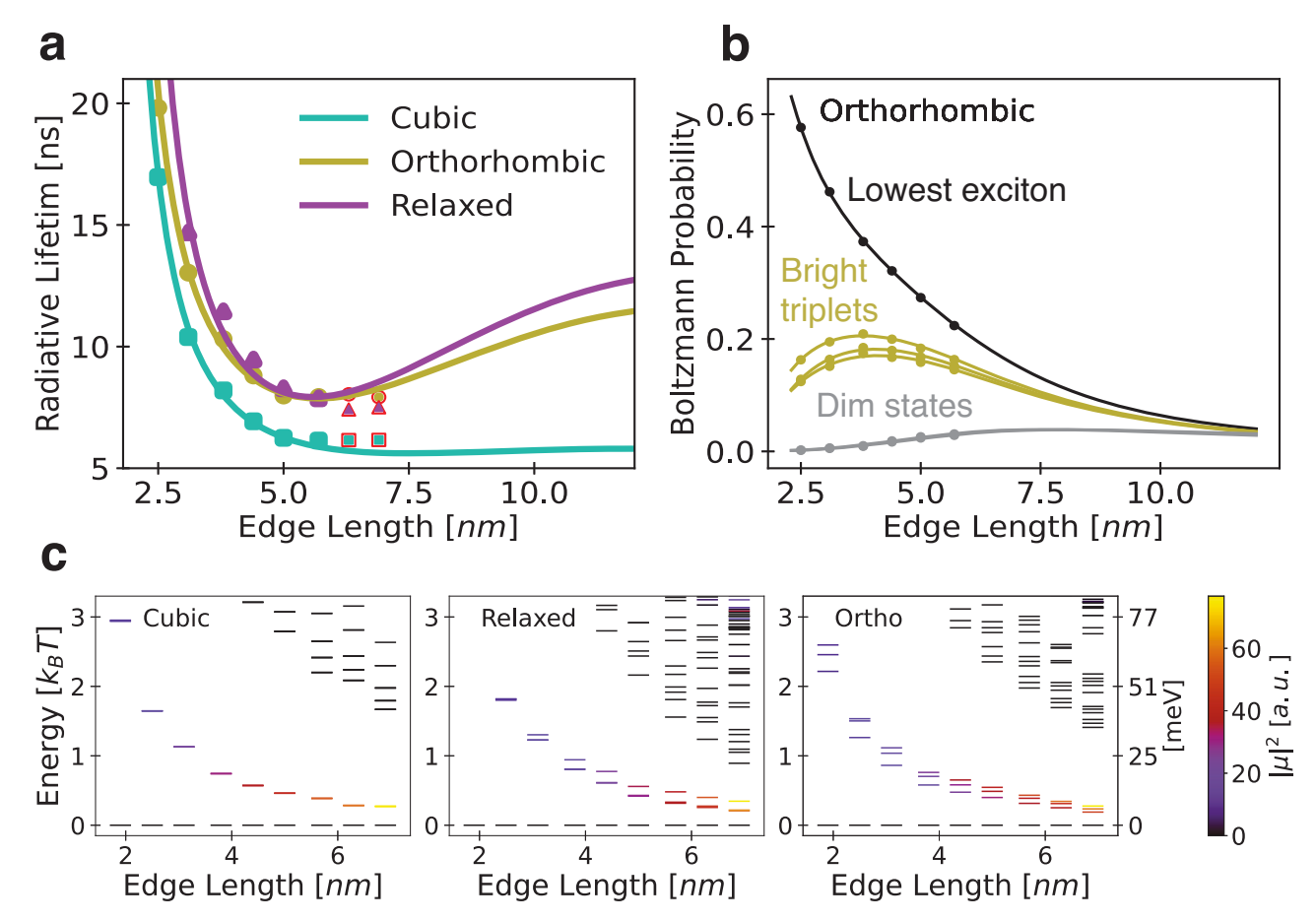


Fig. 5 | **Size-dependent radiative lifetimes calculation. a** Calculated size-dependent radiative lifetimes for cubic (teal squares), relaxed (purple triangles) and orthorhombic (gold circles) CsPbl₃ nanocrystal structures with corresponding radiative lifetime extrapolations from fits of the exciton energies and oscillator strengths (lines). Only the energies and oscillator strengths of the first six sizes are fitted, and the test points (red ringed points) demonstrate non-monotonicity in the radiative lifetimes and fair agreement with the extrapolated trend. **b** Size-dependent Boltzmann probabilities of the dark ground state (black), bright triplet

states (gold), and high-lying dim states (gray) show depopulation of the emissive triplets in large nanocrystals. **c** Calculated excitonic states as a function of nanocrystal size plotted for cubic, orthorhombic, and relaxed structures. Here, states within $3\kappa_B T$ above the lowest exciton levels are visualized. The color of each state encodes indicates the exciton transition dipole square magnitude (proportional to oscillator strength) in atomic units [a.u.], which increases for the bright excitons with increasing nanocrystal size.

and hole product states converges the exciton radiative rates from the BSE, yielding radiative lifetimes that agree well with experiments. A non-monotonic trend in the radiative lifetime is observed as the nanocrystal size increases from the strongly to the intermediately confined regime (Fig. 5a). Uniquely, our atomistic calculations capture this behavior across the size range, showing excellent agreement with experiment for both small and larger perovskite nanocrystals. The lifetime decreases between 2-5 nm, and we rationalize this decrease in radiative lifetime by analyzing the size-dependent oscillator strength of bright states. We find an increase in the oscillator strength of the lowest bright state as the nanocrystals size increases, independently of crystal symmetry (Fig. 5c). However, this does not cause the large nanocrystals approaching weak confinement to exhibit a reduced radiative lifetime. Instead, due to the increasing density of states (DOS) in larger nanocrystals, high-lying states exhibiting weak oscillator strength (i.e., dim states) become thermally accessible and lead to a decreased Boltzmann population of the bright triplet manifold of states (Fig. 5b). We underscore that the non-monotonic behavior depends sensitively on the exciton level details and ambient temperature conditions. We find that at lower temperatures, our model predicts a monotonically decreasing size-dependence of the radiative lifetimes (Supplementary Fig. S8) because the high-lying dim states become thermally inaccessible, in alignment with previously reported experimental findings^{13,15}.

The nanocrystal crystal structure influences the exciton level details. The cubic geometries host degenerate excitons and large bright-dim gaps, while symmetry lowering to the relaxed and orthorhombic structures lifts degeneracies, spreads the excitonic spectrum, and closes the bright-dim gap. In fact, we find that the competition between oscillator strength and thermal depopulation only produces non-monotonicity for the low symmetry structures where the brightdim gap is sufficiently small to compete with the size-dependent oscillator strength increase. We underscore this analysis by constructing a model fit of the size dependent optoelectronic properties. Size-dependent energies and oscillator strengths of excitons in cubic, relaxed, and orthorhombic nanocrystals with 2.5-5.7 nm edge lengths were fitted, and these fitted properties were used to compute the radiative lifetimes (Supplementary Figs. S9-S11). For emphasis, the radiative lifetimes were not fitted. Excitonic states in the BSE framework were calculated for two additional nanocrystals sizes of 6.3 and 6.9 nm (up to 7400 atoms), representing a substantial software development and computational effort due to our inclusion of full spinors, spin-orbit coupling, and open boundary conditions. We capture the non-monotonic turnaround in these test points for both relaxed and orthorhombic geometries, demonstrating that our model is consistent to extrapolate to larger sizes (Fig. 5a). Convergence of the final orthorhombic point proved numerically challenging but is included for completeness. Taking these data together, the interplay of size,

symmetry, and excitonic structure manifests a dramatic nonmonotonicity in lead halide perovskite nanocrystal radiative lifetimes, revealing that CsPbX₃ nanocrystals nearing intermediate confinement show optimal features for applications where rapid photon emission is desirable.

In conclusion, the investigation of the effect of CsPbBr₃ nanocrystal size on radiative lifetime at ambient temperature reveals an unexpected non-monotonic trend. Larger and smaller nanocrystals in the weak and strong quantum confinement regimes displayed longer radiative lifetimes, leaving the intermediately confined nanocrystals to exhibit the shortest radiative lifetimes. Interestingly, we observed a structural symmetry-lowering transition from cubic to orthorhombic symmetry that was supported by X-ray diffraction and MD simulations. The structural transition onset occurs for very small cubic nanocrystals with edge lengths around 2 nm and progresses to the lower symmetry orthorhombic phase as nanocrystal size increases. Simulations of excitons with an atomistic pseudopotential + BSE model revealed that large nanocrystals approaching the weak confinement regime showed extended radiative lifetime due to the thermal population at room temperature of high-lying states with weak oscillator strengths. In contrast, the unexpected lengthening of radiative lifetime in smaller nanocrystals within the strong confined regime was attributed to a significant reduction in oscillator strength, leaving the intermediately confined nanocrystals to exhibit the shortest radiative lifetimes. The observed non-monotonic radiative behavior emerges in orthorhombic and relaxed nanocrystals of lowered structural symmetry due to exciton level splitting that reduces the energy gap from the bright to dim states (bright-dim gap) and increases the density of the lower energy dim states; cubic nanocrystals are not predicted to show nonmonotonic radiative lifetimes. This optoelectronic behavior lends additional support to the XRD measurements and MD simulations, all suggesting that larger perovskite nanocrystals adopt lower symmetry structures. This study emphasizes the intricate and unique interplay between the CsPbBr₃ nanocrystal size and radiative lifetime, paving the way to improve and engineer optical materials with desirable radiative lifetimes for diverse optical applications.

Methods

Chemicals

Lead (II) acetate trihydrate (PbOAc₂•3H₂O, 99.999%), oleylamine (OAm, 70%), 1-octadecene (ODE, 90%), and benzoyl bromide (BzBr, 97%) were purchased from Sigma-Aldrich. Cesium carbonate (Cs₂CO₃, 99.9%, Metal basis) and oleic acid (OA, 90%) were purchased from Thermo Scientific Chemicals. Other chemicals used include anhydrous toluene (99.8%) and hexane.

Synthesis

CsPbBr $_3$ nanocrystals were synthesized following a slightly modified version of previously published procedures 3,37 . Briefly, ODE (10 ml), oleic acid (0.6 ml), oleylamine (2 ml), PbOAc $_2$ (0.4 mmol) and Cs $_2$ CO $_3$ (0.06 mmol) were loaded in a 50 ml round-bottom flask, degassed, and heated at 120 °C for 1 hr. Then, under nitrogen, the temperature was raised to 140 °C for 15 min followed by degassing at 120 °C for 10 min. The injection temperature was then set at 200 °C, under nitrogen, and BzBr (1.7 mmol) solution was injected swiftly. CsPbBr $_3$ nanocrystals formed almost instantly but were allowed to grow for 30–40 sec before quenching in an ice-water bath. The nanocrystals were cleaned in an inert environment via successive precipitation at 10 k rpm without antisolvents and dissolution using toluene. Nanocrystals were stored in 5 ml toluene.

Optical spectroscopy

Absorption spectra were collected using a Shimadzu UV-3600 spectrophotometer. Photoluminescence spectra were acquired on a Horiba Jobin Yvon Fluorolog-3 spectrophotometer equipped with a Synapse

OE-CCD detector. Time-resolved photoluminescence was collected on a Picoquant Fluotime 300 equipped with PMA 175 and an LDH-P-C-405 diode laser with an excitation wavelength of 408 nm. Absolute quantum yield measurements were collected using an integrating sphere coupled with an Ocean Optics QE Pro spectrometer and a 415-nm fibercoupled LED excitation source (M415F3, Thorlabs, 14.4 mW).

XRD

X-ray diffraction patterns were obtained using a Rigaku benchtop X-ray diffractometer that is equipped with HyPix-400 MF 2D hybrid pixel array detector (HPAD) and a Cu K α X-ray source (1.54059 Å) operating at 40 kV and 15 mA.

TEM

TEM and HRTEM images were acquired on an FEI Tecnai T20 S-TWIN TEM operating at 200 kV with a LaB $_6$ filament and equipped with a Gatan Rio 16IS camera with 4 k resolution.

Computational methods

Molecular dynamics simulations as implemented in LAMMPS were performed on CsPbBr₃ and CsPbI₃ nanocubes with edge lengths of 2–6 nm using a Lennard-Jones plus Coulomb force field obtained from Bischak et al.^{32,33}. Force field parameters are provided in the Supplementary Information. Simulations were run in the NVT ensemble using a Langevin thermostat with a damping constant of 100 fs. From an initial temperature of 1 K, the systems were brought up to 300 K by increasing the thermostat temperature by 1 K every 100 fs. Dynamics were evolved for 1 ns of equilibration and 1 ns of subsequent dynamics at 300 K with a 1 fs timestep. The structural symmetry at 300 K was obtained by sampling configurations every 1 ps and averaging the anisotropy order parameter of each sampled configuration according to Eqs. 5 and 6. Structural symmetries at 0 K were computed on relaxed geometries by conjugate gradient minimization of the forces (Supplementary fig. 6).

Electronic excited states were computed in an atomistic quasiparticle plus Bethe-Salpeter equation (BSE) approach. Electron and hole quasiparticle states were computed within the atomistic semiempirical pseudopotential framework³⁴. Local, non-local, and spinorbit terms were included in the pseudopotential, which was fitted to reproduce bandstructures of bulk CsPbI3 at the DFT + GW level. Quasiparticle states are two-component spinors represented on a real space grid with 0.5 Bohr grid spacing in all dimensions. The filter diagonalization technique was utilized to obtain up to 300 singleparticle eigenstates near the band edge. Correlated exciton states were obtained by solving the BSE within the static screening approximation for an electron hole basis of more than 4000 pair states. Massively parallel implementations of filter diagonalization and real-space BSE were developed to enable all-atom simulation of excitons in perovskite nanocrystals ranging from 2-7 nm, up to 7400+ atoms. The source code with example inputs is available on GitHub at https://github.com/ dchabeda/FilterBSE.

Data availability

All the data supporting the findings of this study are available within this article and its Supplementary Information and Source Data file. Any additional information can be requested from corresponding authors. Source data are provided with this paper.

References

- Alivisatos, A. P. et al. Semiconductor clusters, nanocrystals, and quantum dots. Science 271, 933–937 (1996).
- Murray, C. B., Norris, D. J. & Bawendi, M. G. Synthesis and characterization of nearly monodisperse CdE (E = S, Se, Te) semi-conductor nanocrystallites. *J. Am. Chem. Soc.* 115, 8706–8715 (1993).

- Protesescu, L. et al. Nanocrystals of cesium lead halide perovskites (CsPbX3, X = Cl, Br, and I): novel optoelectronic materials showing bright emission with wide color gamut. Nano Lett. 15, 3692–3696 (2015).
- Nenon, D. P. et al. Design principles for Trap-Free CsPbX 3 nanocrystals: enumerating and eliminating surface halide vacancies with softer Lewis bases. J. Am. Chem. Soc. 140, 17760–17772 (2018).
- Koscher, B. A., Swabeck, J. K., Bronstein, N. D. & Alivisatos, A. P. Essentially trap-free CsPbBr3 colloidal nanocrystals by postsynthetic thiocyanate surface treatment. J. Am. Chem. Soc. 139, 6566–6569 (2017).
- Shi, D. et al. Low trap-state density and long carrier diffusion in organolead trihalide perovskite single crystals. Science 347, 519–522 (2015).
- Kang, J. & Wang, L. W. High defect tolerance in lead halide perovskite CsPbBr3. J. Phys. Chem. Lett. 8, 489–493 (2017).
- Cahen, D., Kronik, L. & Hodes, G. Are defects in lead-halide perovskites healed, tolerated, or both?. ACS Energy Lett. 6, 4108–4114 (2021).
- Huang, H., Bodnarchuk, M. I., Kershaw, S. V., Kovalenko, M. V. & Rogach, A. L. Lead halide perovskite nanocrystals in the research spotlight: stability and defect tolerance. ACS Energy Lett. 2, 2071–2083 (2017).
- Huang, H. et al. Colloidal lead halide perovskite nanocrystals: synthesis, optical properties and applications. NPG Asia Mater. 8, e328 (2016).
- Manser, J. S., Christians, J. A. & Kamat, P. V. Intriguing optoelectronic properties of metal halide perovskites. *Chem. Rev.* 116, 12956–13008 (2016).
- Kovalenko, M. V., Protesescu, L. & Bodnarchuk, M. I. Properties and potential optoelectronic applications of lead halide perovskite nanocrystals. Science 358, 745–750 (2017).
- 13. Zhu, C. et al. Single-photon superradiance in individual caesium lead halide quantum dots. *Nature* **626**, 535–541 (2024).
- Zhang, S., Zhukovskyi, M., Jankó, B. & Kuno, M. Progress in laser cooling semiconductor nanocrystals and nanostructures. NPG Asia Materials 11, 54 (2019).
- 15. Becker, M. A. et al. Bright triplet excitons in caesium lead halide perovskites. *Nature* **553**, 189–193 (2018).
- Krieg, F. et al. Monodisperse long-chain sulfobetaine-capped CsPbBr3Nanocrystals and their superfluorescent assemblies. ACS Cent. Sci. 7, 135–144 (2021).
- 17. Ji, Z. & Song, Z. Exciton radiative lifetime in CdSe quantum dots. *J. Semiconductors* **44**, 032702 (2023).
- Donegá, C. D. M. & Koole, R. Size dependence of the spontaneous emission rate and absorption cross section of CdSe and CdTe quantum dots. J. Phys. Chem. C. 113, 6511–6520 (2009).
- Califano, M., Franceschetti, A. & Zunger, A. Temperature dependence of excitonic radiative decay in CdSe quantum dots: The role of surface hole traps. *Nano Lett.* 5, 2360–2364 (2005).
- Leistikow, M. D., Johansen, J., Kettelarij, A. J., Lodahl, P. & Vos, W. L. Size-dependent oscillator strength and quantum efficiency of CdSe quantum dots controlled via the local density of states. *Phys. Rev. B* - Condens. Matter Mater. Phys. 79, 1–9 (2009).
- Brennan, M. C., Kuno, M. & Rouvimov, S. Crystal structure of individual CsPbBr 3 perovskite nanocubes. *Inorg. Chem.* 58, 1555–1560 (2019).
- Beimborn, J. C., Walther, L. R., Wilson, K. D. & Weber, J. M. Size-dependent pressure-response of the photoluminescence of CsPbBr3 nanocrystals. J. Phys. Chem. Lett. 11, 1975–1980 (2020).
- Cottingham, P. & Brutchey, R. L. On the crystal structure of colloidally prepared CsPbBr3 quantum dots. *Chem. Commun.* 52, 5246–5249 (2016).
- Yang, R. X. & Tan, L. Z. Understanding size dependence of phase stability and band gap in CsPbI3 perovskite nanocrystals. *J. Chem. Phys.* 152, 034702 (2020).

- Zhao, Q. et al. Size-dependent lattice structure and confinement properties in CsPbI3 perovskite nanocrystals: negative surface energy for stabilization. ACS Energy Lett. 5, 238–247 (2020).
- Abbas, A. S. et al. Observation of an orientational glass in a superlattice of elliptically-faceted CdSe nanocrystals. ACS Nano 16, 9339–9347 (2022).
- Brennan, M. C. et al. Origin of the size-dependent Stokes shift in CsPbBr3 perovskite nanocrystals. J. Am. Chem. Soc. 139, 12201–12208 (2017).
- Jasrasaria, D. & Rabani, E. Interplay of surface and interior modes in exciton-phonon coupling at the nanoscale. *Nano Lett.* 21, 8741–8748 (2021)
- Rainò, G. et al. Ultra-narrow room-temperature emission from single CsPbBr3 perovskite quantum dots. *Nat. Commun.* 13, 2587 (2022)
- Park, Y. & Limmer, D. T. Biexcitons are bound in CsPbBr3 perovskite nanocrystals. *Phys. Rev. Mater.* 7, 106002 (2023).
- Lin, K. et al. Theory of photoluminescence spectral line shapes of semiconductor nanocrystals. J. Phys. Chem. Lett. 14, 7241–7248 (2023).
- 32. Bischak, C. G. et al. Liquid-like interfaces mediate structural phase transitions in lead halide perovskites. *Matter* **3**, 534–545 (2020).
- 33. Thompson, A. P. et al. LAMMPS a flexible simulation tool for particle-based materials modeling at the atomic, meso, and continuum scales. *Comput Phys. Commun.* **271**, 108171 (2022).
- 34. Weinberg, D., Park, Y., Limmer, D. T. & Rabani, E. Size-dependent lattice symmetry breaking determines the exciton fine structure of perovskite nanocrystals. *Nano Lett.* **23**, 4997–5003 (2023).
- 35. Rohlfing, M. & Louie, S. G. Electron-hole excitations and optical spectra from first principles. *Phys. Rev. B* **62**, 4927 (2000).
- 36. Yang, Z. et al. Impact of the halide cage on the electronic properties of fully inorganic cesium lead halide perovskites. ACS Energy Lett. **2**, 1621–1627 (2017).
- Imran, M. et al. Benzoyl halides as alternative precursors for the colloidal synthesis of lead-based halide perovskite nanocrystals. J. Am. Chem. Soc. 140, 2656–2664 (2018).
- Momma, K. & Izumi, F. VESTA 3 for three-dimensional visualization of crystal, volumetric and morphology data. J. Appl. Crystallogr. 44, 1272–1276 (2011).

Acknowledgements

This work was supported by Samsung Electronics via Samsung Advanced Institute of Technology (SAIT) under Contract No. FRAOO0836. Additional support was provided by the U.S. Department of Energy, Office of Science, Office of Basic Energy Sciences, Materials Sciences and Engineering Division, under Contract No. DEACO2-05-CH11231 within the Fundamentals of Semiconductor Nanowire Program (KCPY23). Computational resources were provided in part by the National Energy Research Scientific Computing Center (NERSC), a U.S. Department of Energy Office of Science User Facility operated under contract no. DEACO2- 05CH11231. This material is based upon work supported by the National Science Foundation Graduate Research Fellowship Program under Grant No. DGE 2146752 (DC). Any opinions, findings, and conclusions or recommendations expressed in this material are those of the author(s) and do not necessarily reflect the views of the National Science Foundation.

Author contributions

A.S.A. conceived this study. A.S.A. synthesized and characterized the nanocrystals and conducted steady-state, time-resolved, TEM, and XRD experiments in consultation with A.P.A. D.C. conceived the mechanistic explanation. D.C. developed the order parameter in consultation with D.T.L. D.C. developed the distributed electronic structure implementations and performed the MD and exciton simulations in consultation with E.R. D.W. developed the perovskite model for the electronic

calculations. A.S.A. and D.C. wrote the paper in consultation with all authors. All authors contributed to the revision of the final paper.

Competing interests

The authors declare no competing interests.

Additional information

Supplementary information The online version contains supplementary material available at https://doi.org/10.1038/s41467-025-60848-5.

Correspondence and requests for materials should be addressed to A. Paul Alivisatos.

Peer review information *Nature Communications* thanks the anonymous reviewers for their contribution to the peer review of this work. A peer review file is available.

Reprints and permissions information is available at http://www.nature.com/reprints

Publisher's note Springer Nature remains neutral with regard to jurisdictional claims in published maps and institutional affiliations.

Open Access This article is licensed under a Creative Commons Attribution-NonCommercial-NoDerivatives 4.0 International License, which permits any non-commercial use, sharing, distribution and reproduction in any medium or format, as long as you give appropriate credit to the original author(s) and the source, provide a link to the Creative Commons licence, and indicate if you modified the licensed material. You do not have permission under this licence to share adapted material derived from this article or parts of it. The images or other third party material in this article are included in the article's Creative Commons licence, unless indicated otherwise in a credit line to the material. If material is not included in the article's Creative Commons licence and your intended use is not permitted by statutory regulation or exceeds the permitted use, you will need to obtain permission directly from the copyright holder. To view a copy of this licence, visit http://creativecommons.org/licenses/by-nc-nd/4.0/.

© The Author(s) 2025